High-Density Well-Aligned Dislocations Introduced by Plastic Deformation in $Bi_{1-x}Sb_x$ Topological Insulator Single Crystals

Yuki Tokumoto *, Riku Fujiwara and Keiichi Edagawa

Institute of Industrial Science, The University of Tokyo, Komaba, Meguro-ku, Tokyo 153-8505, Japan; r-fuji@iis.u-tokyo.ac.jp (R.F.); edagawa@iis.u-tokyo.ac.jp (K.E.)
* Correspondence: tokumoto@iis.u-tokyo.ac.jp; Tel.: +81-3-5452-6324

check for
updates

Abstract: Topological insulators (TIs) have a bulk bandgap and gapless edge or surface states that host helically spin-polarized Dirac fermions. Theoretically, it has been predicted that gapless states could also be formed along dislocations in TIs. Recently, conductivity measurements on plastically deformed bismuth antimony ($Bi_{1-x}Sb_x$) TIs have revealed excess conductivity owing to dislocation conduction. For further application of them, fundamental study on dislocations in TIs is indispensable. Dislocations controlled based on fundamental studies could potentially be useful not only for experimental investigations of the dislocation properties but also for diverse device applications. In the present study, $Bi_{1-x}Sb_x$ TI single crystals were fabricated by a zone-melting method. The crystals were plastically deformed at room temperature. The resultant dislocations were observed by transmission electron microscopy (TEM). It was found that high-density dislocations with the Burgers vector satisfying the condition for the formation of gapless states were successfully introduced. The dislocations were mostly of edge type with lengths on the order of more than a few micrometers.

Keywords: topological insulators; bismuth antimony; single crystals; dislocations; transmission electron microscopy

1. Introduction

Topological insulators (TIs) are characterized by a bulk bandgap and necessarily highly conducting gapless edge or surface states that host helically spin-polarized Dirac fermions [1,2]. These gapless states are protected by time reversal symmetry. Therefore, they are robust against disorder scattering. The verification of three-dimensional (3D) TIs has attracted major attention to the physical properties of surface gapless states. In addition, it has been theoretically shown that gapless states could also be formed along dislocations in 3D TIs satisfying the following condition [3]:

$$
\begin{aligned}
\boldsymbol{b}{\cdot}\mathbf{M} &= \pi \,(\mathrm{mod}\,2\pi), \\
\mathbf{M} &= \tfrac{1}{2}(\nu_1\mathbf{G}_1 + \nu_2\mathbf{G}_2 + \nu_3\mathbf{G}_3),
\end{aligned}
\tag{1}
$$

where $\boldsymbol{b}$ is the Burgers vector of the dislocation, (ν_1, ν_2, ν_3) are the three of the four Z_2 invariants $(\nu_0; \nu_1, \nu_2, \nu_3)$ of the 3D TI [4,5], and $(\mathbf{G}_1, \mathbf{G}_2, \mathbf{G}_3)$ are the reciprocal basis vectors. 3D TIs are characterized by four Z_2 topological invariants $(\nu_0; \nu_1, \nu_2, \nu_3)$. The first invariant, ν_0, defines strong or weak TIs, where $\nu_0 = 1$ corresponds to strong TI (STI) and $\nu_0 = 0$ corresponds to weak TI (WTI). In the case of STI, an odd number of Dirac mode(s) exists on the surface Brillouin zone (BZ) and $\mathbf{M}$, including the latter three invariants, ν_1, ν_2, and ν_3, indicates the location of the Dirac point(s) in the surface BZ. On the other hand, WTI is considered as layers of two-dimensional (2D) TI stacked along $\mathbf{M}$. When the condition in

Equation (1) is satisfied, the surface Dirac particles acquire a π phase shift on crossing the dislocation. Consequently, a topologically protected gapless state is formed along the dislocation.

Similarly to edge states of 2D TIs, which are considered as guided propagation paths of electrons, the dislocations with gapless states are expected to carry dissipationless current. In addition, at high densities of such dislocations, the thermoelectric figure of merit ZT of TI materials can be dominated by one-dimensional (1D) topologically protected conducting states channeled through the dislocations [6]. Thus, the dislocation with gapless states is a candidate for applications in electronic and thermoelectric devices. It should be noted that, in order to satisfy the condition in Equation (1), at least one of the latter three invariants, ν_1, ν_2, or ν_3, must be 1. However, most of the TIs discovered so far, including some of the most-intensively studied $(Bi,Sb)_2(S,Se,Te)_3$ tetradymites, exhibit band inversion at the Γ point; thus, they are classified with the invariants (1;000) [2], where no 1D gapless states along the dislocations can be realized. In contrast, bismuth antimony $(Bi_{1-x}Sb_x)$ TI exhibit band inversion at the L points, and has the invariants (1;111) [7,8]. Thus, it is one of the limited candidates for realization of 1D gapless states along the dislocations.

A $Bi_{1-x}Sb_x$ solid solution is formed in all compositions of $0 < x < 1$. The electronic band structure is drastically modified depending on the composition. It has been known that the solid solution becomes a semiconductor in the composition range $0.07 < x < 0.22$ [9]. In 2006, the semiconductor was predicted to be a TI with the invariants (1;111) [7], which was experimentally verified in the following year [8]. As for the conducting dislocations in TIs, while several theoretical studies have been reported [10–12], no experimental investigations have been reported until recently [13]. Hamasaki et al. performed conductivity measurements on plastically deformed $Bi_{1-x}Sb_x$ TI, which exhibited excess conductivity owing to dislocation conduction [13]. For further use of them in applications, a fundamental study on dislocations in TIs is indispensable. Dislocations controlled based on fundamental studies could potentially be useful not only for experimental investigations of the dislocation properties, but also for diverse device applications.

$Bi_{1-x}Sb_x$ belongs to the rhombohedral A_7 structure. Concerning dislocations in $Bi_{1-x}Sb_x$, the report by Hamasaki et al. [13] is the first and the only one so far. Regarding Bi that has the same crystal structure as $Bi_{1-x}Sb_x$, some studies that used the etch pit method on the dislocations introduced by plastic deformation have been reported [14,15]. However, there are no reports on transmission electron microscopy (TEM) observations of dislocations in Bi, which is mainly due to the difficulty of TEM specimen fabrication, i.e., Bi has a large atomic number; therefore, thinner specimens are required to achieve electron transparency compared to materials with smaller atomic numbers.

In the present study, $Bi_{1-x}Sb_x$ TI single crystals were fabricated by a zone-melting method. The crystals were plastically deformed at room temperature. The resultant dislocations were observed by TEM to reveal the substructure, density, and Burgers vectors.

2. Materials and Methods

$Bi_{1-x}Sb_x$ single crystals were grown by a zone-melting method. First, a mixture of high-purity (6N) Bi and Sb elements, with an Sb concentration of $x = 0.10$, was sealed in an evacuated quartz ampoule with a 7 mm inner diameter. Then, the material was melted and homogenized at 400–450 °C, followed by quenching in ice water. Subsequently, the ingot was subjected to zone melting for crystal growth by using a four mirror infrared furnace (FZ-T-10000-H-HR-TUM-VM-PC, Crystal Systems Co., Ltd., Yamanashi, Japan). The growth velocity was set at 0.1 mm/h to avoid constitutional supercooling resulting in the segregation of Sb. The grown crystal was cut in half along the growth direction to obtain a flat surface. Then, the compositions of the grown crystals were investigated by an electron probe microanalyzer (EPMA) (JXA-8800RL, JEOL Ltd., Tokyo, Japan). For quantitative composition analyses, a melt-spun $Bi_{0.9}Sb_{0.1}$ sample, produced by a single-roller method, was used as a standard for ZAF conversion from the intensities of Bi Lα_1 and Sb Lα_1 to concentrations, where Z is the atomic number factor, A is the absorption factor, and F is the fluorescence factor.

Rectangular samples approximately $1 \times 1 \times 2 \, \text{mm}^3$ in size were cut out and used for the deformation tests. The compression axis and the strain rate were carefully chosen so as to introduce dislocations satisfying the condition in Equation (1). Figure 1 shows the crystallographic orientations of the samples for deformation. The compression axis was set to the $[2\bar{1}\bar{1}]$ direction, in which the primary slip system $(111)\langle 1\bar{1}0 \rangle$ is sufficiently suppressed. According to a previous study that used the etch pit method on the dislocations, which were introduced by plastic deformation of Bi [15], the slip system $(011)[100]$ should be activated with the orientation relationship shown in Figure 1, where the Schmid factor for the slip system $(011)[100]$ and the primary slip systems $(111)\langle 1\bar{1}0 \rangle$ is 0.46 and 0, respectively. Here, it should be noted that $\boldsymbol{b} = \langle 100 \rangle$ satisfies Equation (1), while $\boldsymbol{b} = \langle 1\bar{1}0 \rangle$ does not. Although the $[111]$. direction is another possible compression axis to activate the slip system $\{011\}\langle 100 \rangle$ [13,15], the $[2\bar{1}\bar{1}]$ direction is advantageous to activate a single slip system $(011)[100]$. In our previous study [13], the compression axis was the direction declined by a few degrees from the $[111]$ direction toward the $[\bar{1}11]$ direction, where a single slip system $(011)[100]$ out of the three equivalent slip systems of $\{011\}\langle 100 \rangle$ is activated. However, with the compression axis, as the deformation proceeds, the possibility that other two equivalent slip systems, $(101)[010]$ and $(110)[001]$, are activated increases. Therefore, we consider that the $\langle 2\bar{1}\bar{1} \rangle$ direction is better than the $[111]$ direction to activate a single slip system out of the three equivalent slip systems of $\{011\}\langle 100 \rangle$. The strain rate was set to be approximately $1 \times 10^{-5} \, \text{s}^{-1}$ to avoid twin formation. Twinning deformation easily occurs at a strain rate of $1 \times 10^{-3} \, \text{s}^{-1}$ [16,17] and is suppressed at a strain rate of $1 \times 10^{-4} \, \text{s}^{-1}$ or lower [15,18]. The rectangular samples were deformed by compression at room temperature up to 10%.
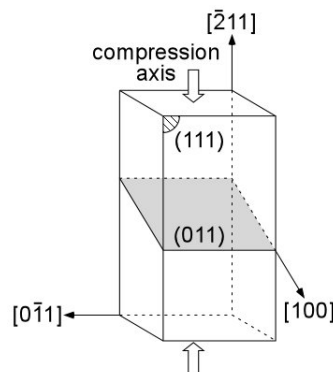

Figure 1. Schematic illustration of the sample for plastic deformations.

The deformed samples were examined by TEM (JEM-2010F, 2010HC, 200 kV, JEOL Ltd., Tokyo, Japan) to identify the substructure, density, and the Burgers vector of the introduced dislocations. The TEM specimens were cut out along the (011) plane and the (111) plane of the deformed samples, and these were further prepared by mechanical thinning and Ar ion milling.

3. Results and Discussion

3.1. Crystal Growth

The grown crystal, 27.5 mm in length and 7 mm in diameter, contained two grain boundaries along the growth direction. Figure 2a,b shows the EPMA line profiles of Sb concentrations obtained for the grown crystal. The line profile in Figure 2a was obtained along the crystal growth direction. In the region between 4.5 mm and 17.5 mm from the tip, the crystal was within the range of the TI phase, $0.07 < x < 0.22$. The line profile in Figure 2b was perpendicular to the growth direction at a position of 13.5 mm from the tip of the grown crystal. Obvious jumps in the profile corresponded to cavities around the grain boundaries. The radial variation in the Sb concentration was about 2%.

Sb concentrations were lower in the center of the crystal than in its outer regions, which could be due to the radial temperature gradient during crystal growth.
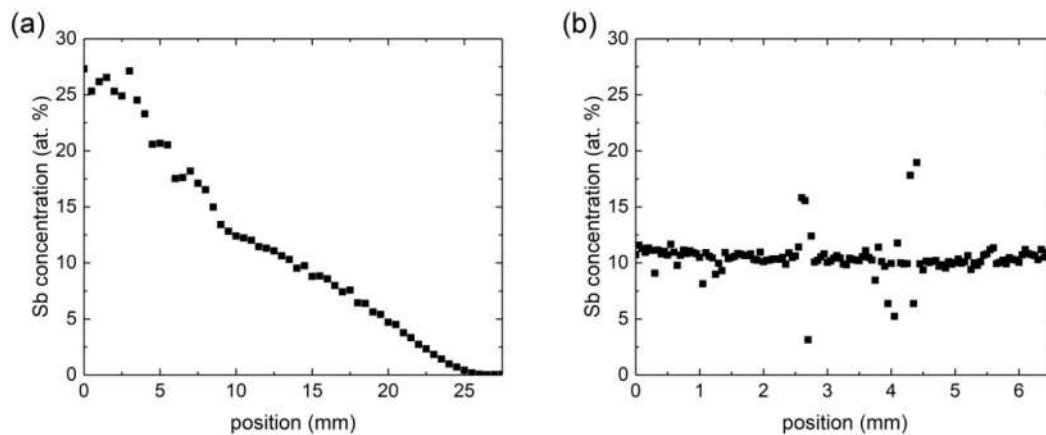
Figure 2. Electron probe microanalyzer (EPMA) line profiles of Sb concentrations obtained for the grown crystal. (**a**) EPMA line profile along the crystal growth direction; (**b**) EPMA line profile perpendicular to the crystal growth direction.

3.2. Plastic Deformation

Figure 3 shows the stress–strain curve obtained from the sample with an Sb concentration in the range of 8.6–9.8 at%. The yield stress was about 60 MPa. This value was an order of magnitude higher than that for the deformation of Bi at room temperature [15,18–20]. This result is consistent with the fact that the interatomic distance of the $Bi_{1-x}Sb_x$ solid solution becomes shorter with increasing Sb concentrations. Work hardening behavior was slightly observed during the initial stage of plastic deformation. Slip traces parallel to the $[\bar{1}00]$ direction were observed on the $(0\bar{1}1)$ surface of the deformed samples. In our previous study [13], where the compression axis declined a few degrees from the $[\bar{1}11]$ direction, obvious work hardening was observed, indicating that possibly more than one equivalent slip systems were activated.
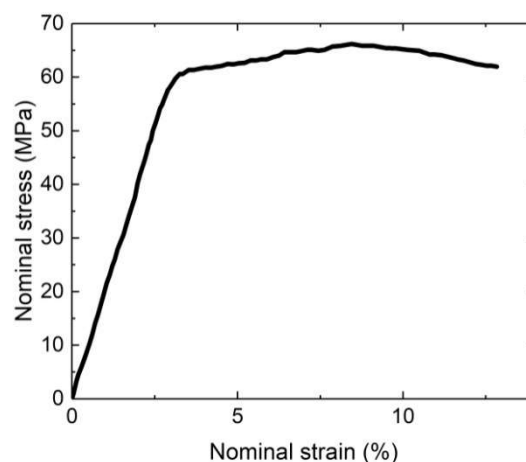

Figure 3. Stress–strain curve of the bismuth antimony ($Bi_{1-x}Sb_x$) sample deformed at room temperature under a constant strain rate of 1×10^{-5} s^{-1}. The Sb concentration of the deformed sample was in the range of 8.6–9.8 at%.

3.3. TEM Observations of Dislocations Introduced by Plastic Deformation

Figure 4a shows typical TEM bright-field images obtained from the (011) slip plane of the deformed sample. The observation direction was tilted from the normal direction of the (011) slip plane by

approximately 10°. Using the convergent-beam technique, the thickness of the TEM specimen was determined to be approximately 100 nm. The total dislocation length observed in the area of 12 μm^2 in Figure 4a was approximately 50 μm. The dislocation density in that area was estimated to be 4×10^9 cm^{-2}. From the extensive TEM observations, the average dislocation density was estimated to be $4-8 \times 10^9$ cm^{-2}. We found that dislocations in the present study were introduced more uniformly throughout the TEM specimen compared with our previous study [13]. The dislocations had long segments along the $[0\bar{1}1]$ direction. Figure 4b shows the same images as in Figure 4a, where dislocations along the $[0\bar{1}1]$ direction are indicated by red lines, while dislocations that deviate from the $[0\bar{1}1]$ direction more than 10° are indicated by blue lines. It was confirmed by tilting the specimen that other contrasts were not dislocations but bend contours. Figure 4c shows a stereographic projection of $Bi_{1-x}Sb_x$. From the measurement of the dislocation lengths, the ratio of the dislocations along the $[0\bar{1}1]$ direction to the total dislocations was determined to be approximately 62%. Here, it should be noted that if the dislocations are randomly directed, the ratio of dislocations along the $[0\bar{1}1]$ direction with $\pm 10^{\circ}$ allowance to the total dislocations becomes 5.5%. As for the dislocations indicated by blue lines, most of them were along the directions 45° tilted from the $[0\bar{1}1]$ direction in the (011) slip plane. As shown in the stereographic projection in Figure 4c, the directions 45° tilted from the $[0\bar{1}1]$ direction in the (011) slip plane are the $[1\bar{1}1]$ and $[\bar{1}11]$ directions.
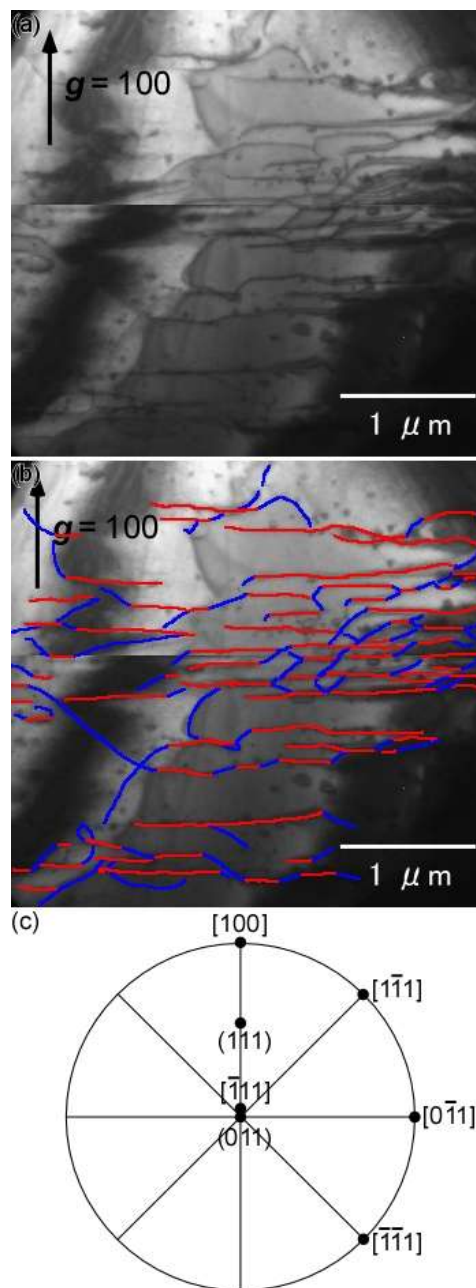
Figure 4. (a) TEM bright-field images obtained from the (011) specimen cut out from the deformed sample; **(b)** the same images as in **(a)**. Dislocations along the $\left[0\bar{1}1\right]$ direction are indicated by red lines and dislocations that deviate from the $\left[0\bar{1}1\right]$ direction more than $10°$ are indicated by blue lines; **(c)** stereographic projection of $Bi_{1-x}Sb_x$.

For **g·b** analyses to investigate the Burgers vector, TEM observations were performed for the ($\bar{1}$11) plane. Figure 5a shows a typical TEM bright-field image obtained from the ($\bar{1}$11) slip plane of the deformed sample. Since the intersection of the ($\bar{1}$11) plane and the (011) slip plane was parallel to the $\left[0\bar{1}1\right]$ direction, straight dislocations along the $\left[0\bar{1}1\right]$ direction were observed. Figure 5b,c shows TEM dark-field images obtained from the same region as in Figure 5a, using $\mathbf{g} = 2\bar{1}\bar{1}$ and $\mathbf{g} = 0\bar{1}1$, respectively. As a result of **g·b** analyses, the contrast of the dislocations vanished with $\mathbf{g} = 0\bar{1}1$. Thus, the Burgers vector was considered to be perpendicular to the $\left[0\bar{1}1\right]$ direction. The primitive translation vector that is perpendicular to the $\left[0\bar{1}1\right]$ direction in the (011) slip plane is

[100]. Consequently, the Burgers vector of the introduced dislocations was determined to be $b = [100]$, which satisfies Equation (1). Dislocations with other Burgers vectors were not found in our TEM observations. This result suggests that longer dislocations with controlled orientations can be obtained by mild plastic deformation without severe work hardening. Since the dislocations had long segments along the $[0\bar{1}1]$ direction, which is perpendicular to the Burgers vector, the observed dislocations were mostly of the edge type. The length of the edge components was approximately a few micrometers. Here, it should be noted that the actual dislocation length could be longer than the observed one because of the difference between the (011) slip plane and the surface of the TEM specimen; the dislocations on the (011) slip plane were inevitably intersected by the surface of the TEM specimen.
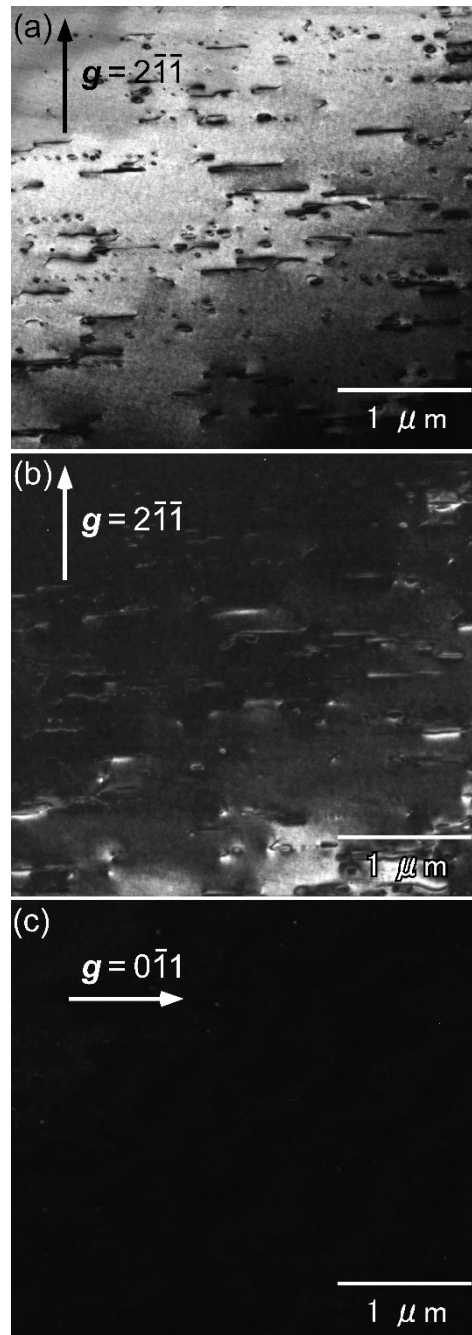
Figure 5. (a) TEM bright-field image obtained from the (111) specimen cut out from the deformed sample; **(b)** TEM dark-field image obtained using $g = 2\bar{1}\bar{1}$; **(c)** TEM dark-field image obtained using $g = 0\bar{1}1$.

The finding that the dislocations were mostly edge dislocations could be interpreted in terms of the Peierls stress. $Bi_{1-x}Sb_x$ with a rhombohedral crystal structure has a cleavage on the (111) plane. Figure 6a,b shows the atomic structure of $Bi_{1-x}Sb_x$ viewed along the $\left[0\bar{1}1\right]$ and $\left[\bar{1}11\right]$ directions, respectively. The $\left[\bar{1}11\right]$ direction is $3°$ tilted from the normal direction of the (011) slip plane toward the [100] direction. Atomic planes parallel to the (111) plane are arranged in double layers as shown in Figure 6a. The interatomic distance in a double layer is shorter than that between adjacent double layers [21]. Therefore, in the (011) plane, the interatomic distance along the [100] direction is larger than that along the $\left[0\bar{1}1\right]$ direction. In addition, it can be assumed that the shorter bonds are stronger and the longer bonds are weaker. Thus, the Peierls stress along the [100] direction should be higher than that along the $\left[0\bar{1}1\right]$ direction. Accordingly, it can be considered that, for mobile dislocations in the (011) plane, the edge segments along the $\left[0\bar{1}1\right]$ direction, which are trapped along the valley of the Peierls potential, require higher stress to glide, thus leading to their lower mobility. In addition, dislocation segments along the $\left[1\bar{1}1\right]$ and $\left[\bar{1}\bar{1}1\right]$ directions observed in Figure 4 are also expected to be stable because they are along the atomic columns as shown in Figure 6b. Resultant long dislocation segments are expected to have an advantage in dislocation conduction measurements. Furthermore, such long dislocations aligned in one direction may be useful for future device applications.
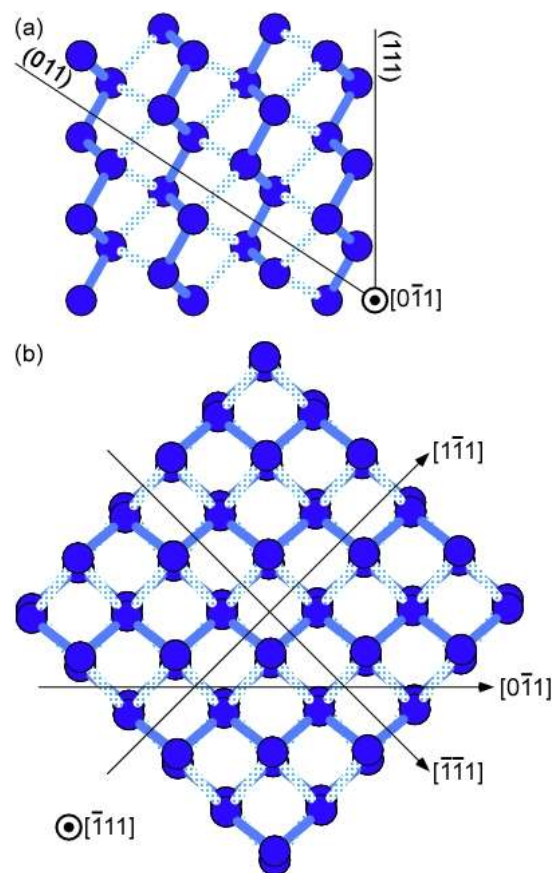
Figure 6. (**a**) Schematic illustration showing the atomic structure of $Bi_{1-x}Sb_x$ viewed along the $\left[0\bar{1}1\right]$ direction; (**b**) schematic illustration showing the atomic structure of $Bi_{1-x}Sb_x$ viewed along the $\left[\bar{1}11\right]$ direction which is $3°$ tilted from the normal direction of the (011) slip plane toward the [100] direction. Shorter and longer bonds are represented by blue and light blue lines, respectively.

4. Conclusions

$Bi_{1-x}Sb_x$ single crystals, within the range of the TI phase with the invariants (1;111), were fabricated by a zone-melting method. The crystals were plastically deformed at room temperature. The compression axis was set at the $[2\overline{1}\overline{1}]$ direction to activate the slip system $(011)[100]$. As a result, high-density dislocations with a Burgers vector $\boldsymbol{b} = [100]$, satisfying the condition for the formation of gapless states, were introduced. The dislocations were mostly of edge type with lengths on the order of more than a few micrometers. For mobile dislocations in the (011) plane, it can be considered that the edge segments along the $[0\overline{1}1]$ direction require higher stress to glide, thus leading to their lower mobility. Resultant long dislocation segments aligned in one direction are expected to have an advantage in experimental investigations of the dislocation properties and future device fabrications.

Conflicts of Interest: The authors declare no conflict of interest.

References

1. Hasan, M.Z.; Kane, C.L. Topological insulators. *Rev. Mod. Phys.* **2010**, *82*, 3045–3067. [CrossRef]
2. Ando, Y. Topological insulator materials. *J. Phys. Soc. Jpn.* **2013**, *82*, 102001. [CrossRef]
3. Ran, Y.; Zhang, Y.; Vishwanath, A. One-dimensional topologically protected modes in topological insulators with lattice dislocations. *Nat. Phys.* **2009**, *5*, 298–303. [CrossRef]
4. Moore, J.E.; Balents, L. Topological invariants of time-reversal-invariant band structures. *Phys. Rev. B* **2007**, *75*, 121306. [CrossRef]
5. Fu, L.; Kane, C.L.; Mele, E.J. Topological insulators in three dimensions. *Phys. Rev. Lett.* **2007**, *98*, 106803. [CrossRef] [PubMed]
6. Tretiakov, O.A.; Abanov, A.; Murakami, S.; Sinova, J. Large thermoelectric figure of merit for three-dimensional topological Anderson insulators via line dislocation engineering. *Appl. Phys. Lett.* **2010**, *97*, 073108. [CrossRef]
7. Fu, L.; Kane, C.L. Topological insulators with inversion symmetry. *Phys. Rev. B* **2007**, *76*, 045302. [CrossRef]
8. Hsieh, D.; Qian, D.; Wray, L.; Xia, Y.; Hor, Y.S.; Cava, R.J.; Hasan, M.Z. A topological Dirac insulator in a quantum spin Hall phase. *Nature* **2008**, *452*, 970–974. [CrossRef]
9. Ellett, M.R.; Horst, R.B.; Williams, L.R.; Cuff, K.F. Shubnikov-de Haas investigations of the $Bi_{1-x}Sb_x$ ($0 < x < 0.3$) system. *J. Phys. Soc. Jpn.* **1996**, *21*, 666–672.
10. Imura, K.; Takane, Y.; Tanaka, A. Weak topological insulator with protected gapless helical states. *Phys. Rev. B* **2011**, *84*, 035443. [CrossRef]
11. Yoshimura, Y.; Matsumoto, A.; Takane, Y.; Imura, K. Perfectly conducting channel on the dark surface of weak topological insulators. *Phys. Rev. B* **2013**, *88*, 045408. [CrossRef]
12. Slager, R.-J.; Mesaros, A.; Juricic, V.; Zaanen, J. Interplay between electronic topology and crystal symmetry: Dislocation-line modes in topological band insulators. *Phys. Rev. B* **2014**, *90*, 241403. [CrossRef]
13. Hamasaki, H.; Tokumoto, Y.; Edagawa, K. Dislocation conduction in Bi-Sb topological insulators. *Appl. Phys. Lett.* **2017**, *110*, 092105. [CrossRef]
14. Otake, S.; Motohashi, Y. Plastic deformation and dislocation etch-pit distribution for the primary glide system on bismuth single crystals. *J. Jpn. Inst. Met. Mater.* **1973**, *37*, 44–51. [CrossRef]
15. Motohashi, Y.; Otake, S. Plastic deformation and dislocation etch-pit distribution due to the glide system for bismuth single crystals. *J. Jpn. Inst. Met. Mater.* **1973**, *37*, 978–985. [CrossRef]
16. Yanaka, Y.; Kariya, Y.; Watanabe, H.; Hokazono, H. Plastic deformation behavior and mechanism of bismuth single crystals in principal axes. *Mater. Trans.* **2016**, *57*, 819–823. [CrossRef]

17. Yanaka, Y.; Kariya, Y.; Watanabe, H.; Hokazono, H. Influence of temperature on plastic deformation behavior and mechanism of bismuth single crystals. *J. Electron. Mater.* **2018**, *47*, 594–603. [CrossRef]

18. Otake, S.; Namazuea, H.; Matsuno, N. Critical resolved shear stresses of two slip systems in bismuth single crystals. *Jpn. J. Appl. Phys.* **1980**, *19*, 433–437. [CrossRef]

19. Steegmuller, C.; Daniel, J.S. Slip in bismuth. *J. Less Common Met.* **1972**, *27*, 81–85. [CrossRef]

20. Matsuo, T.; Suzuki, H. Effect of plastic deformation on the thermal conductivity of bismuth crystals. *J. Phys. Soc. Jpn.* **1976**, *41*, 1692–1698. [CrossRef]

21. Mooser, E.; Peason, W.B. The crystal structures and properties of the group VB to VIIB elements and of compounds formed between them. *J. Phys. Chem. Solids* **1958**, *7*, 65–77. [CrossRef]